catalysts

MDPI

Article

Ultrasound-Assisted Photocatalytic Degradation of Azo Dyes under Visible Light Irradiation Using Polythiophene-Decorated $CoFe_2O_4$ Nanohybrids

Kristen Hauser, Sara Ou Hassou and Ufana Riaz *

Department of Chemistry and Biochemistry, North Carolina Central University, Durham, NC 27701, USA
* Correspondence: uriaz@nccu.edu

Abstract: The present work reports the synthesis of cobalt ferrite and its nanohybrids with polythiophene (PTh) in the weight ratios of 10% and 20%. The ferrite and its nanohybrids were characterized using thermogravimetric analysis (TGA), X-ray diffraction (XRD), X-ray photoelectron spectroscopy (XPS) and scanning electron microscopy coupled with elemental mapping (Fe-SEM) to confirm the morphology as well as the structure of the synthesized nanohybrids. The nanohybrids were tested for their photocatalytic activity upon modification of PTh against Alizarin Yellow (AY), Congo Red (CR) and Brilliant Blue (BB). Almost 100% degradation was achieved in 30 min using 50 mg of the photocatalyst. The effect of catalyst concentration and dye concentration was also investigated to explore optimum concentration of the photocatalyst required for rapid degradation of the dye. The generation of radicals responsible for degradation was analyzed by radical scavenging experiments and a probable mechanism of degradation was proposed.

Keywords: photocatalysis; cobalt ferrite; polythiophene; degradation kinetics

Citation: Hauser, K.; Hassou, S.O.; Riaz, U. Ultrasound-Assisted Photocatalytic Degradation of Azo Dyes under Visible Light Irradiation Using Polythiophene-Decorated $CoFe_2O_4$ Nanohybrids. *Catalysts* **2024**, *14*, 495. https://doi.org/10.3390/catal14080495

Academic Editor: Bo Weng

Received: 26 June 2024
Revised: 29 July 2024
Accepted: 29 July 2024
Published: 31 July 2024

1. Introduction

Conventional photocatalysts such as TiO_2 and ZnO have been extensively investigated in the field of photocatalysis, but their application has been restricted due to their large bandgaps that are mostly active under ultraviolet (UV) light [1,2]. One of the methods commonly adopted to reduce the bandgap and enhance the photocatalytic performance has been the utilization of transition metal oxide heterostructures such as MnO_2 [3], Cu_2O [4,5], Fe_2O_3 [6] Co_2O_3 [7], NiO [8], CuO [9], etc., exhibiting large surface area, chemical stability, and enhanced photocatalytic activity [10]. Nanostructured spinel ferrites have emerged as the most studied photocatalytic materials in recent years due to their narrow bandgap, which allows rapid degradation of organic pollutants under visible light [11]. Spinel ferrites have their two distinct tetrahedral and octahedral structures where the divalent metal cations (Zn^{2+}, Cd^{2+}, Co^{2+}, Mg^{2+} and Cu^{2+}) occupy the tetrahedral sites, and the trivalent metal cations (Fe^{3+}, Al^{3+}, Eu^{3+}) occupy the octahedral sites [12]. Hence, the unique crystal lattice provides extra catalytic sites that lead to enhancement in the photocatalytic activity under visible light irradiation. The other features that make these materials a subject of immense interest are their ease of synthesis, chemical stability, and ease of recovery, as they are magnetically separable, thereby promoting green photocatalytic technology [13,14].

To enhance the visible light activity and prevent electron–hole recombination, nanocomposites/nanohybrids of the spinel ferrites have been formulated with conducting polymers (CPs) such as polyaniline (PANI) [15], poly(1-naphthylamine (PNA) [16], p(o-phenylene diamine) (POPD) [17], polythiophene (PTh) [18], etc. CPs are known to act as sensitizers and can degrade the pollutants due to an increase in the mobility of charge carriers upon visible light excitation. Although a lot of work has been reported on cobalt ferrite-based nanohybrids with CPs, no work has been reported on the formulation of its nanohybrids with PTh [19,20].

Hence, with a view to explore the effect of PTh loading on the photocatalytic performance of $CoFe_2O_4$ nanohybrids, the present work reports the synthesis and characterization of PTh/$CoFe_2O_4$ nanohybrids using 10 wt.% and 20 wt.% loading of PTh. The loading of the CP was confirmed by thermogravimetric analysis (TGA) via char content, while the synergistic interaction of PTh with cobalt ferrite was established by X-ray photoelectron spectroscopy (XPS) analysis. The X-ray diffraction (XRD) experiments confirmed the crystallinity of the nanohybrids and the crystal structure of cobalt ferrite. The ultrasound-assisted photocatalytic degradation was studied using three dyes: Congo Red (CR), Alizarin Yellow (AY) and Brilliant Blue (BB). The effect of dye concentration and photocatalyst concentration was also analyzed and the radicals responsible for degradation of these dyes were confirmed by radical scavenging experiments. A tentative mechanism of photocatalysis was proposed.

2. Results

2.1. Confirmation of Loading of PTh via Thermogravimetric Analysis (TGA) Studies

The TGA profile of $CoFe_2O_4$, shown in Figure 1, showed 5% weight loss around 300 °C and 20% weight loss around 600 °C. The TGA profile of PTh showed 30% weight loss around 300 °C and complete weight loss at 600 °C. The TGA profile of 10-PTh/$CoFe_2O_4$ exhibited 15% weight loss at 400 °C, while 30% weight loss was found at 600 °C. Based on the difference in the weight loss profiles of pristine PTh and $CoFe_2O_4$, the char content at 600 °C was 10 wt.%, which confirmed the loading of PTh to be 10 wt.% in this case. Likewise, the TGA profile of 20-PTh/$CoFe_2O_4$ showed 20% weight loss around 375 °C and 40 wt.% loss was found at 600 °C, which confirmed the loading of PTh to be 20% in this nanohybrid. Hence, the char content of the nanohybrids confirmed the loading of PTh in $CoFe_2O_4$.

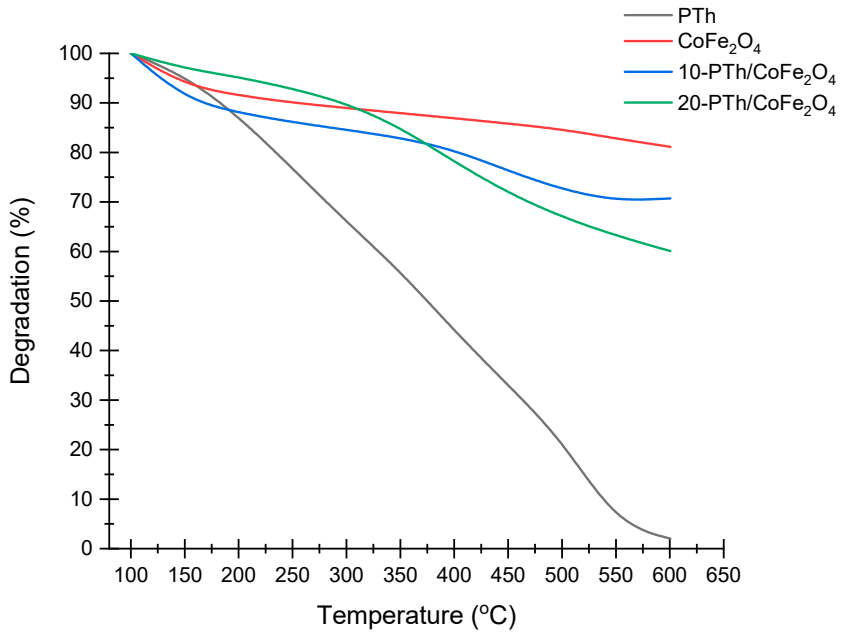

Figure 1. TGA of $CoFe_2O_4$ and PTh/$CoFe_2O_4$ nanohybrids.

2.2. XRD Analysis

The XRD profile of $CoFe_2O_4$, shown in Figure 2, showed peaks at 2θ = 32.3°, 33.6°, 38°, 41.5° and 58.3° corresponding to (220), (222), (311), (440), (400) planes respectively. The structural phase of $CoFe_2O_4$ was confirmed to be face-centered cubic (FCC) with lattice parameters of a = b = c = 8.3 A° and a = b = c = 90° cobalt ferrite (file No. 22-1086) and space group of Fd-3m based on the standards of JCPDS. The XRD of 10-PTh/$CoFe_2O_4$ and 20-PTh/$CoFe_2O_4$ exhibited a peak at 2θ = 25.2°, which was correlated to the presence of

PTh. Interestingly, the nanohybrids revealed all peaks associated with $CoFe_2O_4$ with minor changes in intensity, confirming that the crystalline structure of $CoFe_2O_4$ remained intact and PTh encapsulated the ferrite structure, as reported by other authors [21–23].

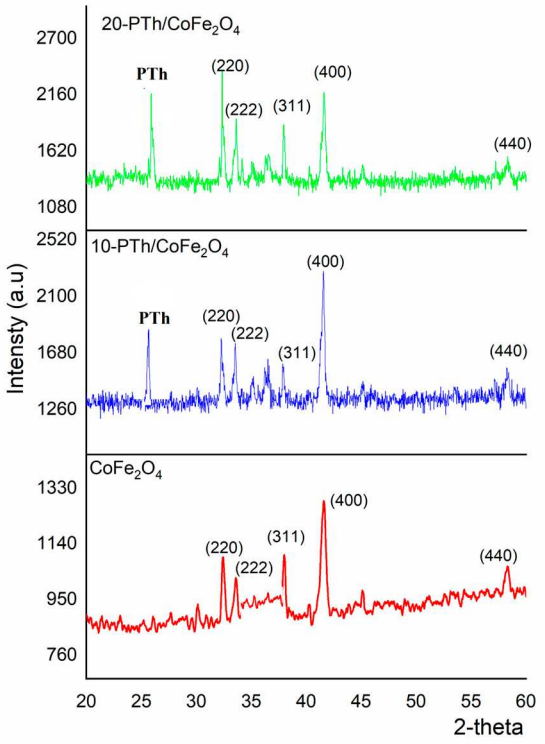

Figure 2. XRD of $CoFe_2O_4$ and PTh/$CoFe_2O_4$ nanohybrids.

2.3. XPS Analysis

The XPS profile of $CoFe_2O_4$ and PTh/$CoFe_2O_4$ nanohybrids is provided in Supporting Information as Figure S1a–h. The survey spectra showed peaks corresponding to Co (1s), Fe (2p ½ and 2p $^{3/2}$), C (1s) and S (2p). The high-resolution spectrum of $CoFe_2O_4$ revealed Fe 2p peaks at binding energy 710.35 eV and a broad hump at 724 eV assigned to Fe $2p^{1/2}$ and Fe $2p^{3/2}$, respectively. These results support the presence of Fe^{3+} in the invers spinel $CoFe_2O_4$. The nanohybrids 10/PTh/$CoFe_2O_4$ and 20-PTh/$CoFe_2O_4$ also revealed the Fe 2p peaks at 710.37 and 710.47, respectively [24,25]. Minor shifting in binding energy was noticed along with the change in the full width at half maxima (FWHM) values, confirming synergistic interaction of PTh with $CoFe_2O_4$ via electrostatic interaction. The core-level C1s XPS spectrum of the nanohybrids revealed peaks at binding energies 289.17 eV, 284.50 eV and 286.16 eV assigned to C-S, C=C and C-C, respectively. There was an appreciable increase noticed in the C-S FWHM values for 20-PTh/$CoFe_2O_4$, which confirmed the presence of a higher amount of PTh and hence higher extent of interaction between the S of PTh with the Fe as well as Co in $CoFe_2O_4$ present in the nanohybrid. Likewise, the high resolution of S 2p in 10-PTh/$CoFe_2O_4$ exhibited a single peak at 169 eV associated with the S in PTh, with FWHM value of 1.29, which increased to 2.12 for 20-PTh/$CoFe_2O_4$. The shifting of peaks and changes in the FWHM values indicated strong interaction between the polymer and the metal ferrite.

2.4. SEM with Elemental Mapping

The SEM of $CoFe_2O_4$, shown in Figure 3a, shows a granular morphology comprising Co, Fe, and O. The SEM of 10-PTh/$CoFe_2O_4$, shown in Figure 3b, also revealed a granular morphology, exhibiting intense bright particles and confirming higher concentration of O and S, while the SEM of 20-PTh/$CuFe_2O_4$, shown in Figure 3c, revealed mainly S content to be predominant, which enveloped the $CoFe_2O_4$ particles, thereby confirming

the encapsulation of ferrite by the polymer [25,26]. The elemental mapping shows an increase in the C, O and S content surface in both of the nanohybrids (given in Supporting Information as Figure S2a–c). The surface was found to be S-rich and O-rich, as compared to the pristine metal ferrite, indicating that PTh was intimately mixed with $CoFe_2O_4$ and mostly covered the surface of the metal ferrite.

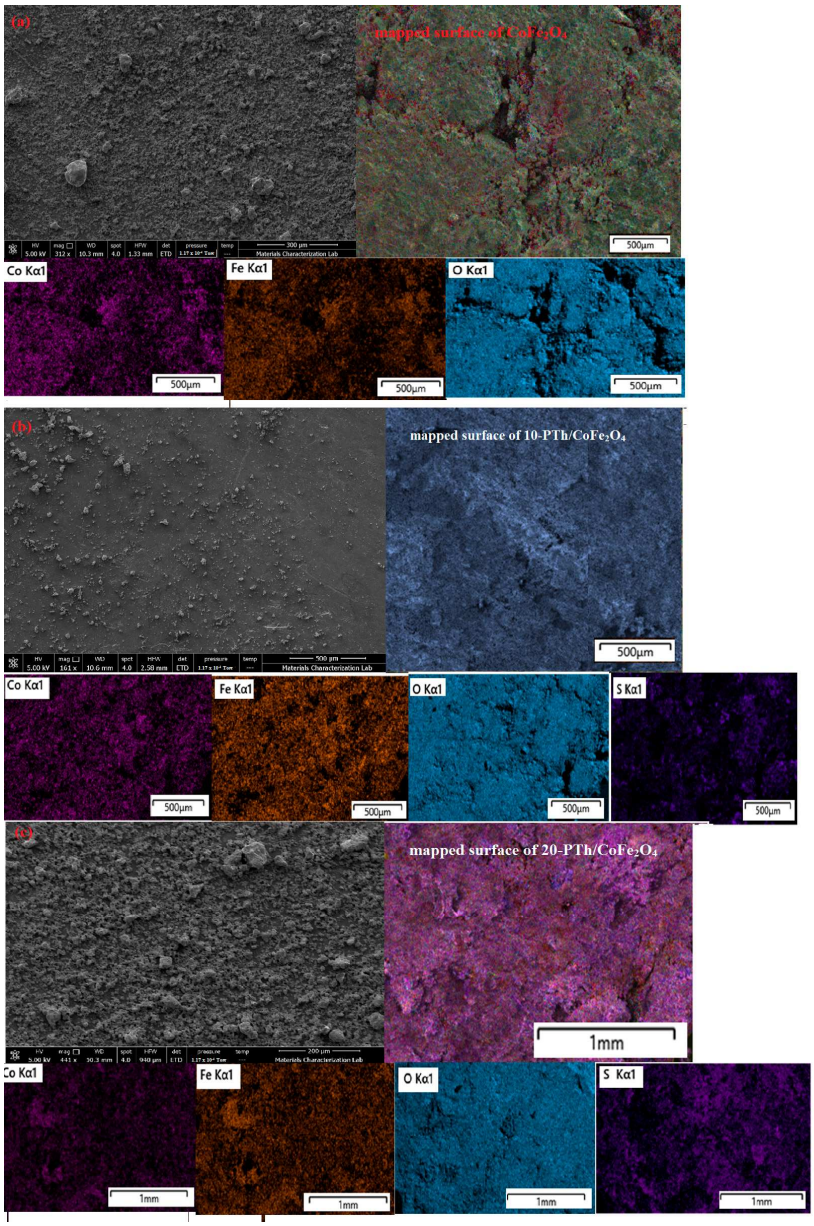

Figure 3. SEM with elemental mapping of (**a**) $CoFe_2O_4$, (**b**) 10-PTh/$CoFe_2O_4$, (**c**) 20-PTh/$CoFe_2O_4$ nanohybrids.

2.5. Analysis of Bandgap

The optical band gaps of $CoFe_2O_4$ and PTh/$CoFe_2O_4$ nanohybrids were calculated using Kubelka–Munk equation and are shown in Figure 4a–c [25,26]. The band gap for pristine $CoFe_2O_4$ was found to be 1.77 eV [27]. The band gap values were found to be 1.55 eV for 10/PTh/$CoFe_2O_4$ and 1.45 eV for 20-PTh/$CoFe_2O_4$, suggesting that with an increase in PTh loading, the band gap consistently reduced. In a conducting polymer/metal ferrite nanohybrid, CP acts as a photosensitizer to absorb a wide range of visible light because of the lower bandgap compared to metal ferrite. Polymers like PTh, poly ethylene dioxythiophene (PEDOT), usually have a non-degenerate ground state but show three

distinct electronic band structures upon doping due to the formation of polaron by local changes in the structure when the polymer gets oxidized. In our case, ferric chloride was used as an initiator as well as dopant. Hence, a double-charged bipolaron is formed in PTh due to loss of electrons, and by further oxidation, the bipolarons overlap, forming bipolaronic bands, thereby reducing the overall bandgap and functioning as a sensitizer for the metal ferrite [27].

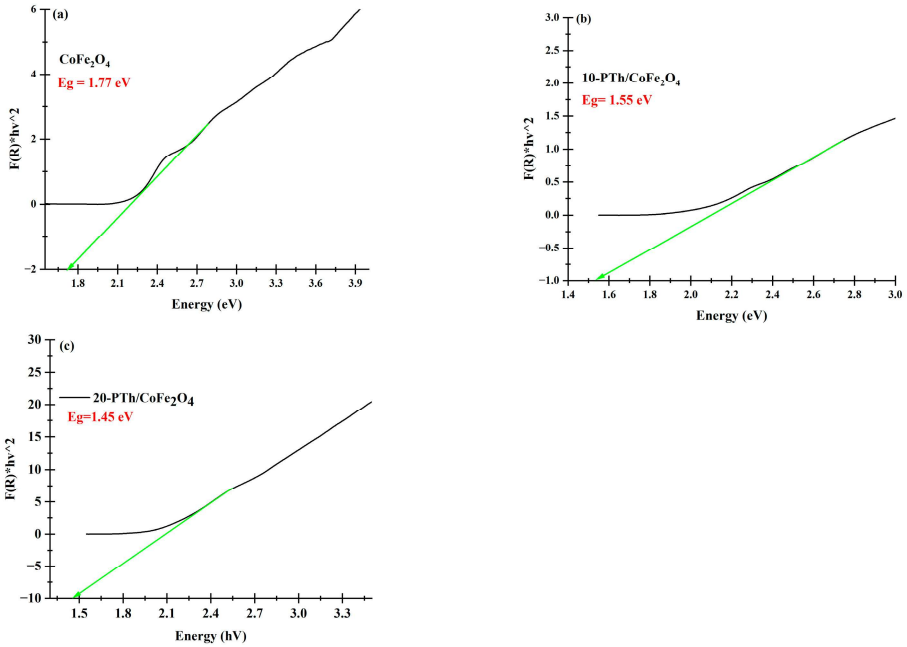

Figure 4. Kubelka–Munk plot of (**a**) $CoFe_2O_4$ (**b**) 10-PTh/$CoFe_2O_4$, (**c**) 20-PTh/$CoFe_2O_4$.

2.6. Photocatalytic Activity

The adsorption of dyes played an important role in degradation, and for this purpose, the Langmuir adsorption data were plotted with amount of dye, Qe, as a function of the equilibrium concentration of dye in the solutions.

The data followed the Langmuir isotherm as per the following equation:

$$\frac{C_e}{Q_e} = \frac{C_e}{Q_m} + \frac{1}{k^2 Q_m} \quad (1)$$

where Ce is the concentration of the dye at equilibrium, k^2 is the Langmuir adsorption constant expressed in mL/mg and Q_m is the adsorption capacity in mg of dye per mg of catalyst.

The second-order model for adsorption is given as:

$$\frac{dq_t}{dt} = ks\ (Qe - Qt)^2 \quad (2)$$

where Q_t is the amount adsorbed at time t (in mg of dye/mg of catalyst) and ks is the rate constant (mg of catalyst/mg of dye). Integrating Equation (2) for qt = 0 at t = 0, we obtain:

$$\frac{1}{q_t} = \frac{1}{K_s Q_e} + \frac{1}{Q_e}\, t \quad (3)$$

A linear plot of t/Qt vs. t for various dyes was obtained and the values of Qm, Qe, and $KsQe^2$ were determined from the slope; they are given in Table 1. It shows that there was slight adsorption of dyes onto $CoFe_2O_4$ particles, but for the PTh/$CoFe_2O_4$ nanohybrids, which showed an increase with the increase in the amount of PTh. This

was due to the development of electrostatic interaction between the anionic dyes (AY) and (CR) and the cationic dye (BB) with PTh. There was slightly higher adsorption of anionic dyes, as the negatively charged groups of the dyes showed higher interactions with the positively charged backbone of PTh, while the cationic dye BB presumably showed repulsion, resulting in its lower adsorption as compared to the anionic dyes [28].

Table 1. Kinetic parameters for the adsorption of AY, BB, CR by $CoFe_2O_4$ and PTh/$CoFe_2O_4$.

Adsorption Parameters	$CoFe_2O_4$	10-PTh/$CoFe_2O_4$	20-PTh-$CoFe_2O_4$
AY-dye			
Qm	0.103	0.111	0.115
Qe	0.032	0.038	0.042
$KsQe^2$	0.041	0.044	0.048
CR-dye			
Qm	0.112	0.120	0.135
Qe	0.045	0.058	0.062
$KsQe^2$	0.051	0.064	0.068
BB-dye			
Qm	0.005	0.112	0.131
Qe	0.015	0.018	0.020
$KsQe^2$	0.012	0.016	0.022

The photocatalytic activity of $CoFe_2O_4$ and PTh/$CoFe_2O_4$ nanohybrids was studied against Brilliant Blue, Alizarin Yellow and Congo Red dyes. The C/Co plots of the dyes using 50 mg of $CoFe_2O_4$ and PTh/$CoFe_2O_4$ nanohybrids and 50 ppm dye concentration are shown in Figure 5a–c. For $CoFe_2O_4$, 80% degradation of BB dye was observed, as shown in Figure 5a, using 50 mg of the photocatalyst, while for 10/PTh, 85% degradation was attained using the same amount of the photocatalyst, as shown in Figure 5b. Almost 98% degradation was achieved using 20-PTh/$CoFe_2O_4$. Similarly, for the AY dye, using $CoFe_2O_4$ achieved 83% degradation, and 86% degradation was attained using 10/PTh/$CoFe_2O_4$, as shown in Figure 5b, while 97.3% degradation was seen for 20-PTh/$CoFe_2O_4$. For the CR dye, as shown in Figure 5c, $CoFe_2O_4$ exhibited 74% degradation, while 20-PTh/$CoFe_2O_4$ exhibited 85% degradation. The degradation kinetics followed the pesudo-first order kinetics model in all cases.

2.7. Effect of Catalyst Concentration and Dye Concentration

To study the effect of catalyst concentration, 25 mg to 100 mg of $CoFe_2O_4$ and PTh/$CoFe_2O_4$ was used against 60 ppm dyes, as shown in Figure 6a–c. For BB, AY and CR dyes, as shown in Figure 6a–c) maximum degradation was achieved using 150 mg. For the BB dye, as shown in Figure 6a, $CoFe_2O_4$ exhibited maximum degradation of 88% using 150 mg of the 10-PTh/$CoFe_2O_4$ and 20-PTh/$CoFe_2O_4$ photocatalyst, while 10-PTh/$CoFe_2O_4$ showed 95% degradation using the same amount of catalyst. The nanohybrid 20-PTh/$CoFe_2O_4$ showed 100% degradation using 150 mg of the photocatalyst. For the AY dye, as shown in Figure 6b, $CoFe_2O_4$ showed 90% degradation using 150 mg of the photocatalyst, while 10-PTh/$CoFe_2O_4$ and 20-PTh/$CoFe_2O_4$ showed 96% and 100% degradation, respectively, using the same amount of the photocatalyst. For the CR dye, as shown in Figure 6c, $CoFe_2O_4$, 10-PTh/$CoFe_2O_4$ and 20-PTh/$CoFe_2O_4$ showed maximum degradation of 88%, 93% and 100%, respectively. The degradation of the dyes was higher using 100 mg of the catalyst and 150 mg of the catalyst concentration.

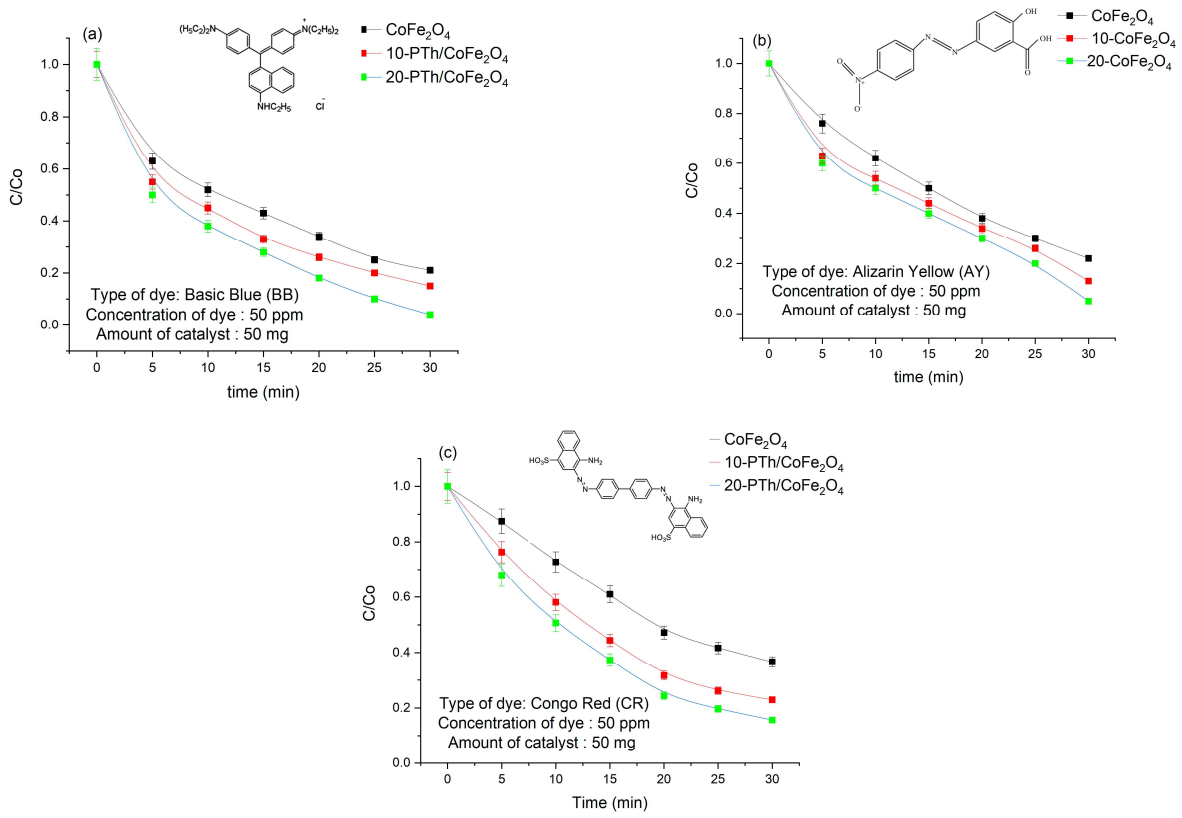

Figure 5. C/Co plots for (**a**) BB dye, (**b**) AY dye and (**c**) CR dye.

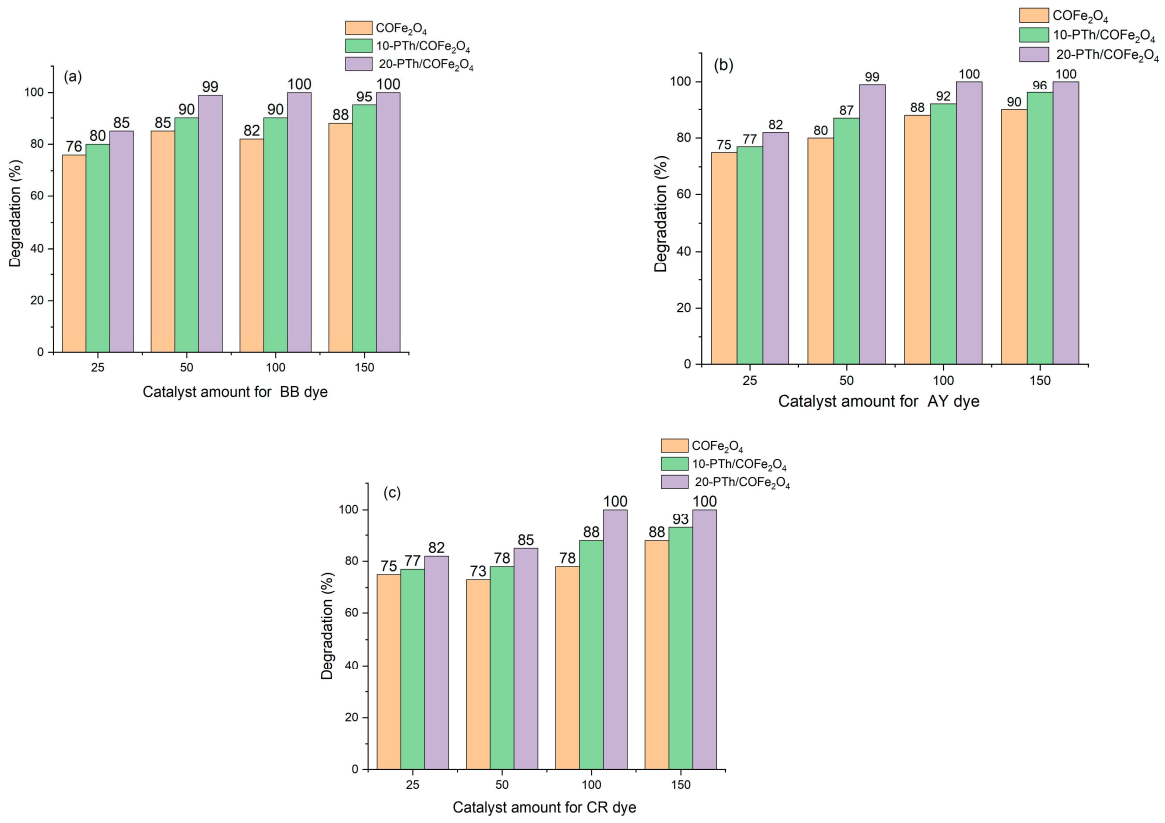

Figure 6. Effect of catalyst concentration on the degradation of (**a**) BB dye, (**b**) AY dye and (**c**) CR dye.

To study the effect of dye concentration, 50 ppm, 100 ppm and 150 ppm of BB, AY and CR dyes were used along with 100 mg of the $CoFe_2O_4$ and PTh/$CoFe_2O_4$ photocatalyst, as shown in Figure 7a–c. Values of 85%, 90% and 100% degradation were achieved using 50 ppm BB dye with $CoFe_2O_4$, 10-PTh/$CoFe_2O_4$, and 20-PTh/$CoFe_2O_4$, as shown in Figure 7a. Likewise, for 50 ppm AY dye, as shown in Figure 7b, maximum degradation of 80%, 87% and 99% was seen using $CoFe_2O_4$, 10-PTh/$CoFe_2O_4$, and 20-PTh/$CoFe_2O_4$, respectively, while 73%, 78% and 85% degradation of the CR dye was observed using $CoFe_2O_4$, 10-PTh/$CoFe_2O_4$, and 20-PTh/$CoFe_2O_4$, respectively, as shown in Figure 7c. Among all the dyes, a lower degradation rate was seen for the CR dye as compared to the BB and AY dyes, presumably due to the higher conjugation and molar mass of the dye.

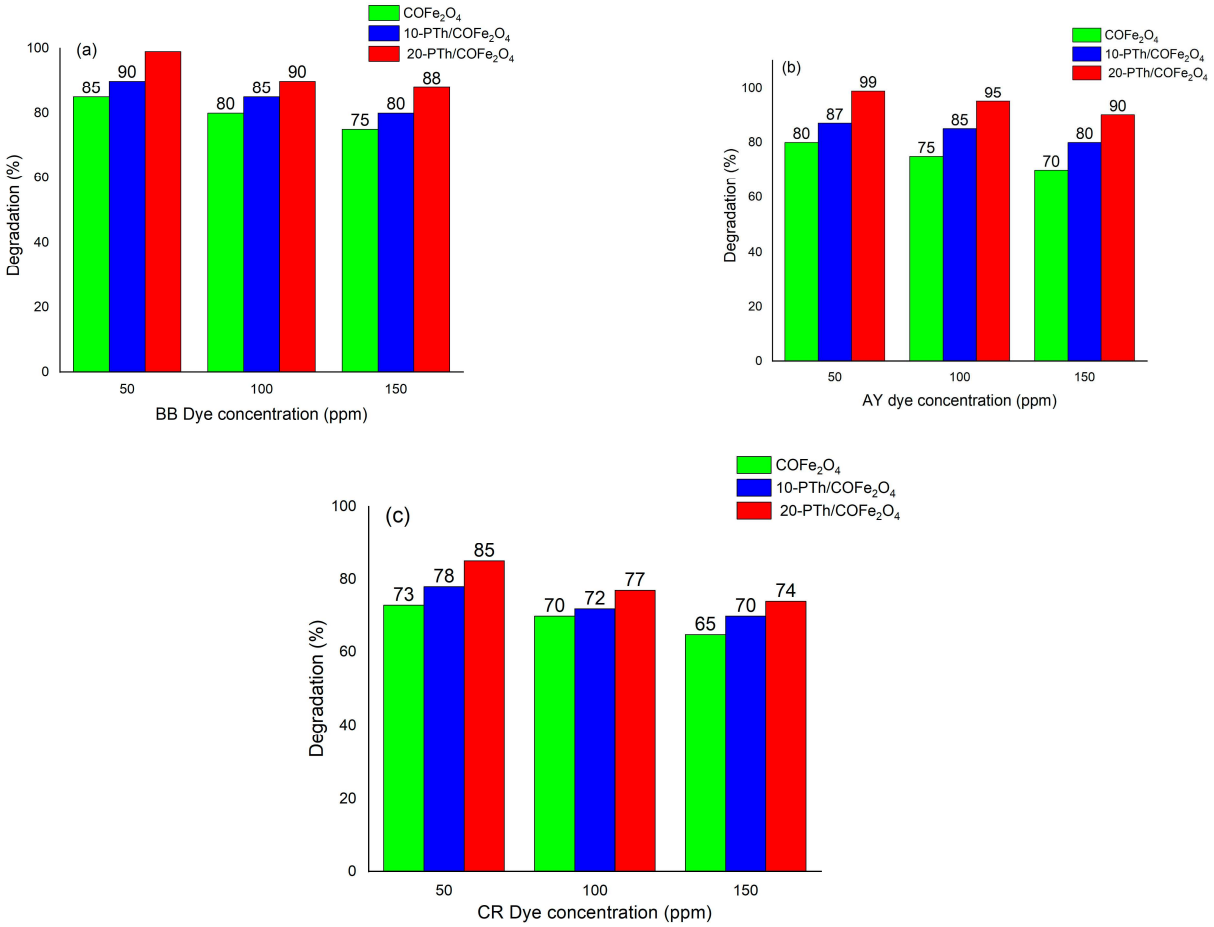

Figure 7. Effect of dye concentration on the degradation for (**a**) BB dye, (**b**) AY dye and (**c**) CR dye.

2.8. Radical Scavenging Experiments

To further explore the generation of radicals responsible for photocatalytic degradation of dyes, radical scavenging studies were carried out to confirm the main reactive oxidative species involved in the photocatalytic degradation of the of the dyes [16]. The use of radical scavengers leads to a decrease in the rate of photocatalytic activity if the targeted radical is involved actively in the mechanism. Tertiary butyl alcohol (t-BuOH) has been widely used as a hydroxyl radical scavenger ($^{\bullet}OH$), whereas formic acid, ethylenediaminetetraacetic acid (EDTA), and ammonium oxalate had been used as a hole scavenger (h^+). p -Benzoquinone and Cu^{2+} are widely used as superoxide radicals ($O_2^{\bullet-}$) and electrons (e−) scavengers, respectively. Before being exposed to visible irradiation, the BB, AY and CR dye solutions were mixed with various scavengers, ethylene diamine tetra acetic acid (EDTA) (h+ scavenger), Na_2SO_4 (oxygen scavenger) and t-butyl alcohol (t-BuOH), which is an $^{\bullet}OH$ scavenger, as shown in Figure 8. The degradation efficiency in all cases was

reduced to 35–40% in the presence of t-BuOH, confirming that hydroxyl radicals were the min species involved in the degradation of the dyes in the presence of $CoFe_2O_4$, and PTh/$CoFe_2O_4$ nanohybrids, as photocatalysts. Ghosh et al. [29] studied the photo response of PEDOT nanofibers decorated with Au nanoparticles under visible light and established that holes, hydroxyl radicals, and superoxide radicals were the reactive species involved in the enhanced photocatalytic activity of PEDOT/Au hybrids.

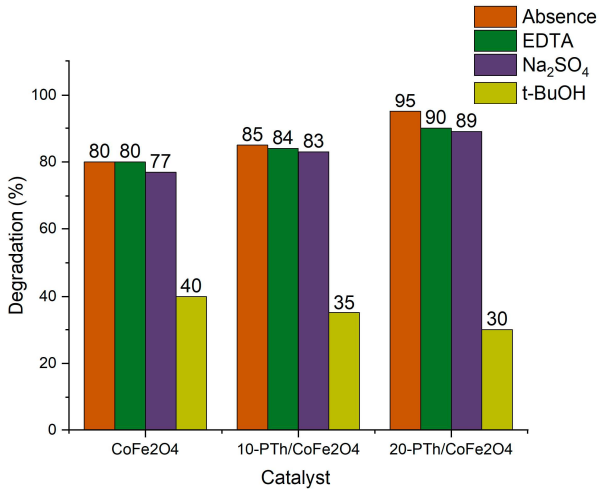

Figure 8. Effect of addition of radical scavenger on the degradation rate.

2.9. Mechansim of Degradation

The photocatalytic mechanism is presented in Scheme 1. When visible light irradiates the PTh, a photon with energy higher than the bandgap excites an electron from the highest occupied molecular orbital (HOMO) to the lowest unoccupied molecular orbital (LUMO), also known as the π- $\pi*$ electronic transition [30]. CP acts as a photosensitizer to absorb a wide range of visible light because of the lower bandgap compared to metal ferrite, and the LUMO of PTh injects electrons (e^-) into the conduction band (CB) of the metal ferrite, which reacts with an adsorbed water molecule to form $O_2{}^{-\bullet}$ radicals, whereas holes may react with water to form $^\bullet$OH [31–33]. Higher generation of $^\bullet$OH radicals causes the degradation of the dyes [31]. The overall mechanism can be depicted as follows:

1. CP + *hv* (visible light) $\rightarrow$CP (e^- (*LUMO*) . . .h^+ (*HO*MO);
2. Electron (e^-) + $O_2 \rightarrow O_2{}^{-\bullet}$ (superoxide radical);
3. $O_2{}^{-\bullet}$ + H^+ (from H_2O) $\rightarrow{}^\bullet$OOH;
4. $2{}^\bullet OOH \rightarrow O_2 + H_2O_2$;
5. $H_2O_2 + O_2{}^{-\bullet} \rightarrow {}^\bullet OH + OH^- + O_2$;
6. $H_2O_2 + h^+ \rightarrow 2\ HO^\bullet$.

The PTh thus acts as a sensitizer towards the metal ferrite and replenishes the electrons and holes in its valence and conduction bands and prevents their recombination.

The combination of PTh with the metal ferrite leads to a reduction in the band gap, as confirmed by UV-DRS experiments, which suggested that heterojunctions are created, and it is known that thiophene-based polymers have smaller band gaps as compared to the other five membered heterocycles. The lower bandgap causes photoinduced charge transfer under visible light irradiation from the lowest unoccupied molecular orbital (LUMO) of PTh to the conduction band of the metal ferrite with holes remaining in PTh. This phenomenon thus prevents electron–hole recombination. The extended π-conjugation in PTh facilitates charge transport. The other factors that can possibly cause higher photocatalytic activity are enhancement in the surface area as well as increase in the surface-active sites for photocatalysis upon nanohybrid formation. As seen in the SEM elemental mapping, the hybrid surface is rich in O and S, which possibly creates highly reactive sites for photocatalysis.

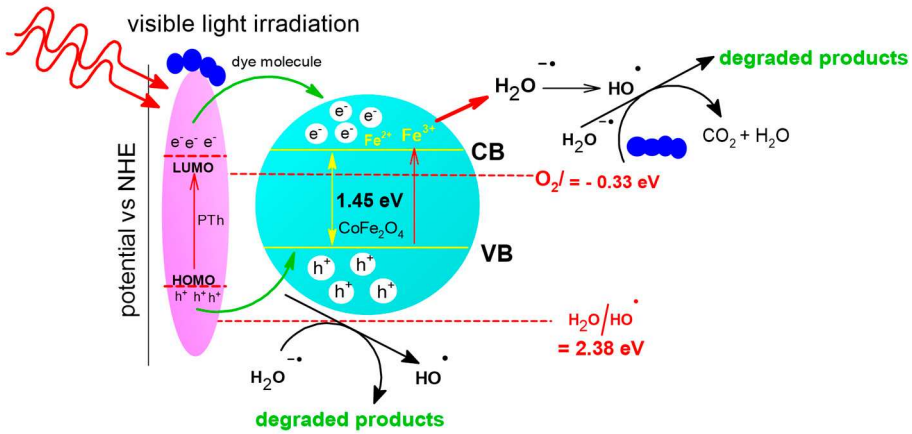

Scheme 1. Mechanism of photocatalytic activity by PTh/metal ferrite nanohybrid.

Table 2 compares the photocatalytic activity with other polymer/metal ferrites. Leng et al. [34] designed PANI-modified $CoFe_2O_4$-TiO_2 nanoarchitectures and studied the photocatalytic degradation of methylene blue (MB) dye in aqueous using UV and visible light. They obtained complete degradation under UV light within 60 min, while under visible light, complete degradation was obtained after 180 min. They explained the mechanism of degradation by showing that polyaniline (PANI) and cobalt ferrite both absorbed photons to generate electron–hole pairs and the photogenerated electrons in the LUMO of PANI were injected into the conduction band (CB) of TiO_2, and then transferred to the CB of $CoFe_2O_4$, due to which rapid charge separation and slow charge recombination occurred. Sadeghpour et al. [35] investigated the photocatalytic stability of PANI/$CoFe_2O_4$ against azo dyes Acid Black, Congo Red, Acid Blue, and Acid Violet and obtained 80%, 90% 85% and 90% degradation under visible light. The authors showed that cobalt ferrite had no major role in the photocatalytic process but was easy to collect due to its magnetic behavior, while it was PANI that was excited under visible light to generate electronic charges as well as radicals responsible for degradation. In our previous work, we have reported 100% degradation of Malachite Green under visible light irradiation using poly(o-phenylenediamine) and cobalt ferrite nanohybrids. The higher extent of degradation within a short span of 100 min was attributed to the synergistic interaction between the polymer and metal ferrite [25]. Jung et al. [36] also studied the degradation of Methyl Orange under visible light using $Co_{0.5}Mn_{0.5}Fe_2O_4$-PANI nanohybrids and achieved 92% degradation within 120 min. These authors too showed that it was PANI that was excited under visible light to generate electron and holes and electrons were transferred from the LUMO of PANI to the CB of $Co_{0.5}Mn_{0.5}Fe_2O_4$, while the holes formed in $Co_{0.5}Mn_{0.5}Fe_2O_4$ were injected into the HOMO of PANI. Hence, the heterojunction structure of PANI and $Co_{0.5}Mn_{0.5}Fe_2O_4$ caused decomposition of the dye due to its large surface area, as well as enhanced photoinduced separation. We have also shown the synergistic effect of PTh and $CoFe_2O_4$ that leads to rapid photocatalytic degradation of the dyes within a short span of 30 min.

Table 2. Comparison of photocatalytic activity of conducting polymer/$CoFe_2O_4$-based materials.

Photocatalyst (Concentration)	Pollutant (Concentration)	Light Source	Duration	Degradation (%)
PANI-$CoFe_2O_4$-TiO_2 (1 g/L) [34]	Methylene Blue (50 mg/L MB)	UV light Light visible 500 W Xe for Visible and 11 W, 0.8 mW/cm^2 for UV	60 min 180 min	>99% (UV) 99% (visible_)

Table 2. *Cont.*

Photocatalyst (Concentration)	Pollutant (Concentration)	Light Source	Duration	Degradation (%)
$CoFe_2O_4$/PANI (0.5 g) [35]	Acid Black, Congo Red Acid Blue, Acid Violet (20 mL)	UV and visible light	30 min	80% 90% 85% 90%
$CoFe_2O_4$/poly(o-phenylenediamine) (POPD) (200 mg) [25].	MG dye (200 ppm)	Visble light	100 min	100%
$Co_{0.5}Mn_{0.5}Fe_2O_4$-PANI (0.02 g) [36]	Methyl orange 0.02 g L^{-1}. (100 mL)	Visble light	120 min	92%
PTh/$CoFe_2O_4$ our work	BB,AY,CR (20 ppm 300 mL)	Visible light	30 min	99%

3. Experimental Methods and Characterization

Cobalt nitrate $Co(NO_3)_2{\cdot}6H_2O$ and ferric nitrate $Fe(NO_3)_3$, $9H_2O$ (Merck, Wilson, NC, USA), thiophene (Merck, Wilson, NC, USA), ferric chloride (Merck, Wilson, NC, USA) were used without further purification.

3.1. Synthesis of Polythiophene

Thiophene monomer (10 mL) was dissolved in deionized water (30 mL) and placed in a 150 mL conical flask and sonicated for 30 min. $FeCl_3$ (1 g) dissolved in deionized water (30 mL) was added drop-wise to the thiophene solution for a period of half an hour and the mixture was sonicated at 25 °C for 4 h on an ultrasonic bath/magnetic stirrer. The obtained polymer was then centrifuged and washed with deionized water to remove the unreacted monomer, oxidant and other impurities and finally dried in a vacuum oven at 80 °C for 24 h.

3.2. Synthesis of $CoFe_2O_4$

Cobalt nitrate and ferric nitrate were used without further purification. Initially, Cobalt nitrate $Co(NO_3)_2{\cdot}6H_2O$ (0.1 M) and $Fe(NO_3)_3$. $9H_2O$ (0.2 M) were dissolved in 100 mL of distilled water separately and stirred to obtain a lucid solution. Then, mineralizer (NaOH) was added drop-wise in line to achieve pH 9 under continuous stirring, and finally, the obtained precipitate was stirred at 80 °C for 3 h. As a result, brown precipitate was centrifuged thrice with double-distilled water and twice with ethanol. The obtained product was dried at 80 °C for 24 h in an oven, followed by calcination at 500 °C to a further period of 5 h to obtain the final product of $CoFe_2O_4$ nanoparticles.

3.3. Preparation of Nanohybrids

For the preparation of 10-PTh/$CoFe_2O_4$, PTh (10 mg) was dispersed in deionized water along $CoFe_2O_4$ (100 mg) and grinded using an agate mortar pestle for 3 h followed by drying in a vacuum oven at 70 °C for 24 h. A similar procedure was adopted for the synthesis of 20-PTh/$CoFe_2O_4$.

3.4. UV–Visible Studies

Diffuse reflectance spectroscopy (Perkin-Elmer Lamda-365+, Shelton, CT, USA) was used to measure the UV–Vis reflectance spectra of synthetic materials. The wavelength range was from 200 to 800 nm.

3.5. XPS Analysis

XPS experiments were performed using a Physical Electronics Versa Probe III instrument equipped with a monochromatic Al kα x-ray source (hν = 1486.6 eV) and a concentric hemispherical analyzer. Charge neutralization was performed using both low-energy electrons (<5 eV) and argon ions. The binding energy axis was calibrated using sputter-cleaned Cu (Cu 2p3/2 = 932.62 eV, Cu 3p3/2 = 75.1 eV) and Au foils (Au 4f7/2 = 83.96 eV).† Peaks were charge referenced to the CHx band in the carbon 1 s spectra at 284.8 eV. Measurements were collected at a takeoff angle of 45° with respect to the sample surface plane. This resulted in a typical sampling depth of 3–6 nm (95% of the signal originated from this depth or shallower). Quantification was performed using instrumental relative sensitivity factors (RSFs) that account for the x-ray cross-section and inelastic mean free path of the electrons. On homogeneous samples, major elements (>5 atom%) tend to have standard deviations of <3%, while minor elements can be significantly higher. The analysis size was ~200 µm in diameter.

3.6. XRD Studies

X-ray diffraction patterns were obtained using a Malvern Panalytical Empyrean® Mastersizer 3000+ Ultra, X-ray diffractometer coupled with Ni-filtered Cu-Kα radiation.

3.7. SEM Studies

Field emission–scanning electron microscopy (FE-SEM) was used to analyze the surface morphology using Leo Supra 50 V P, Carl Zeiss, Oberkochen, Germany.

3.8. Adsorption Studies

Adsorption experiments were conducted by adding different amounts of metal ferrite and PTH/metal ferrite hybrid into the flask containing 50 mL of dye solutions with an initial concentration of 20 mg/L under magnetic stirring for 2 h in the dark. Samples were collected at different time intervals (0, 5, 10, 20, 30 min, respectively) and concentration of the dye was determined by Perkin-Elmer Lambda 30 UV–vis spectrophotometer. The dye concentrations were calibrated using the Beer–Lambert law at λ_{max} values of AY, CR and BB dyes.

3.9. Dye Degradation Studies

Approximately 50 mg of catalyst was dispersed in CR, AY and BB dye solutions (50 ppm, 300 mL) and the adsorption–desorption equilibrium between the dye solution and the catalyst was established by keeping it under dark condition for 3 h. The solution was then exposed to visible light irradiation for 60 min and aliquots of the solution (5 mL) were taken and centrifuged at regular intervals of 0, 10, 20, 30, 40, 50, and 60 min. The UV spectra of the solutions were taken on a Perkin-Elmer Lambda 30 UV–Vis spectrophotometer.

3.10. Radical Scavenging Experiments and Recyclability Tests

For scavenging studies, 5 mM concentrations of scavengers were used for the detection of $^{\bullet}$OH radicals, holes (h+), and electrons (e−), as reported in our previous studies, respectively [12,13]. The scavengers were gradually introduced to the dye solution containing the catalyst to observe how scavengers affected the rate of degradation. The collected samples were washed with distilled water and dried in a vacuum oven for about 6 h at 80 °C.

4. Conclusions

PTh-decorated $CoFe_2O_4$-based nanohybrids were successfully synthesized and the loading of the conducting polymer was confirmed by thermogravimetric measurements. The XRD studies confirmed the structure to be crystalline and the loading of PTh did not alter the crystallinity of the nanohybrids. XPS showed changes in the FWHM values, which confirmed the interaction between PTh and $CoFe_2O_4$. SEM with elemental mapping confirmed encapsulation of the $CoFe_2O_4$ with PTh. The Kubelka–Munk plots

showed lower bandgap values for the nanohybrids as compared to pristine metal ferrite. The photocatalytic activity showed rapid degradation of dyes using 20-PTh/$CoFe_2O_4$ nanohybrids. The degradation rate was found to be highest for all the dyes in presence of PTh/$CoFe_2O_4$ as compared to pristine $CoFe_2O_4$. The nanohybrids could be utilized as effective photocatalysts for the degradation of azo dyes. Studies on the rate of degradation of a mixture of dyes in the presence of $CoFe_2O_4$ are under progress in our laboratory and will be published soon.

Supplementary Materials: The following supporting information can be downloaded at: https://www.mdpi.com/article/10.3390/catal14080495/s1, Figure S1 (a) XPS survey spectrum of $CoFe_2O_4$ and PTh/$CoFe_2O_4$, high resolution spectra of (b) Fe 2p in $CoFe_2O_4$, (c) Fe 2p in 10-PTh/$CoFe_2O_4$, (d) Fe 2p in 20-PTh/$CoFe_2O_4$, (e) C 1s in 10-PTh/$CoFe_2O_4$, (f) C 1s in 20-PTh/$CoFe_2O_4$, (g) S 2p in 10-PTh/$CoFe_2O_4$, (h) S 2p in 20-PTh/$CoFe_2O_4$. Figure S2 Elemental mapping of (a) $CoFe_2O_4$ (b) 10-PTh/$CoFe_2O_4$, (c) 20-PTh/$CoFe_2O_4$.

Author Contributions: Conceptualization, U.R.; methodology, S.O.H.; software, K.H.; validation, U.R.; formal analysis, S.O.H.; investigation, K.H.; resources, U.R.; data curation, K.H.; writing—original draft preparation, S.O.H.; writing—review and editing, U.R.; supervision, U.R.; project administration, U.R.; All authors have read and agreed to the published version of the manuscript.

Funding: National Science Foundation (Award # 2122044), the NSF PREM for Hybrid Nanoscale Systems between NCCU and Penn State for providing financial assistance.

Data Availability Statement: The data presented in this study are available in Supplementary Materials.

Conflicts of Interest: The authors declare no conflict of interest.

References

1. Karajz, D.A.; Szilágyi, I.M. Review of photocatalytic ZnO nanomaterials made by atomic layer deposition. *Surf. Interfaces* **2023**, *40*, 103094. [CrossRef]
2. Riaz, U.; Ashraf, S.M.; Kashyap, J. Role of Conducting Polymers in Enhancing TiO_2-based Photocatalytic Dye Degradation: A Short Review. *Polym.-Plast. Technol. Eng.* **2015**, *54*, 1850–1870. [CrossRef]
3. Chiam, S.L.; Pung, S.Y.; Yeoh, F.Y. Recent developments in MnO_2-based photocatalysts for organic dye removal: A review. *Environ. Sci. Pollut. Res.* **2020**, *27*, 5759–5778. [CrossRef] [PubMed]
4. Kangralkar, M.V.; Momin, N.; Manjanna, J. Cu_2O nanoparticles for adsorption and photocatalytic degradation of methylene blue dye from aqueous medium. *Environ. Nanotechnol. Mon. Manag.* **2019**, *12*, 100265.
5. Ajmal, A.; Majeed, I.; Malik, R.N.; Iqbal, M.; Nadeem, M.A.; Hussain, I.; Zeshan, Y.S.; Mustafa, G.; Zafar, M.I.; Nadeem, M.A. Photocatalytic degradation of textile dyes on Cu_2O-CuO/TiO_2 anatase powders. *J. Environ. Chem. Eng.* **2016**, *4*, 2138–2146. [CrossRef]
6. Halfadji, A.; Chougui, A.; Djeradi, R.; Ouabad, F.Z.; Aoudia, H.; Rajendrachari, S. TiO_2-Decorated by Nano-γ-Fe_2O_3 as a Catalyst for Efficient Photocatalytic Degradation of Orange G Dye under Eco-friendly White LED Irradiation. *ACS Omega* **2023**, *8*, 39907–39916. [CrossRef] [PubMed]
7. Amrin, A.R. Photocatalytic oxidation of Congo Red dye by using Co_2O_3–Cr_2O_3 as a Photocatalyst. *Mesop. Environ. J.* **2016**, *2*, 66–74.
8. Far, H.; Hamici, M.; Brihi, N.; Haddadi, K.; Boudissa, C.; Chihi, T.; Fatmi, M. High-performance photocatalytic degradation of NiO nanoparticles embedded on α-Fe_2O_3 nanoporous layers under visible light irradiation. *J. Mater. Res. Technol.* **2022**, *19*, 1944–1960. [CrossRef]
9. Raizada, P.; Sudhaik, A.; Patial, S.; Hasija, V.; Khan, A.A.P.; Singh, P.; Gautam, S.; Kaur, M.; Nguyen, V.-H. Engineering nanostructures of CuO-based photocatalysts for water treatment: Current progress and future challenges. *Arab. J. Chem.* **2020**, *13*, 8424–8457. [CrossRef]
10. Krishnan, A.; Swarnalal, A.; Das, D.; Krishnan, M.; Saji, V.S.; Shibli, S.M.A. A review on transition metal oxides based photocatalysts for degradation of synthetic organic pollutants. *J. Environ. Sci.* **2024**, *139*, 389–417. [CrossRef]
11. Gaffar, S.; Kumar, A.; Riaz, U. Synthesis techniques and advance applications of spinel ferrites: A short review. *J. Electroceram.* **2023**, *51*, 246–257. [CrossRef]
12. Shah, P.; Unnarkat, A.; Patel, F.; Shah, M.; Shah, P. A comprehensive review on spinel based novel catalysts for visible light assisted dye degradation. *Proc. Saf. Environ. Protect.* **2022**, *161*, 703–722. [CrossRef]
13. Fouladi, A.A.; Falak, P.; Tabrizi, S.A.H. The photodegradation of antibiotics on nano cubic spinel ferrites photocatalytic systems: A review. *J. Alloys Compd.* **2023**, *961*, 171075. [CrossRef]
14. Riaz, U.; Ashraf, S.M.; Aqib, M. Microwave-assisted degradation of acid orange using a conjugated polymer, polyaniline, as catalyst. *Arab. J. Chem.* **2014**, *7*, 79–86. [CrossRef]

15. Riaz, U.; Ashraf, S.M.; Budhiraja, V.; Aleem, S. Comparative studies of the photocatalytic and microwave–assisted degradation of alizarin red using ZnO/poly (1-naphthylamine) nanohybrids. *J. Mol. Liq.* **2016**, *216*, 259–267. [CrossRef]
16. Zia, J.; Riaz, U. Photocatalytic degradation of anti-inflammatory drug using POPD/Sb_2O_3 organic-inorganic nanohybrid under solar light. *J. Mater. Res. Technol.* **2019**, *8*, 4079–4093. [CrossRef]
17. Zia, J.; Fatima, F.; Riaz, U. A comprehensive review on the photocatalytic activity of polythiophene-based nanocomposites against degradation of organic pollutants. *Catal. Sci. Technol.* **2021**, *11*, 6630–6648. [CrossRef]
18. Zia, J.; Riaz, U. Photocatalytic degradation of water pollutants using conducting polymer-based nanohybrids: A review on recent trends and future prospects. *J. Mol. Liq.* **2021**, *340*, 117162. [CrossRef]
19. Zia, J.; Rafi, M.; Aazam, E.S.; Riaz, U. Microwave—Assisted catalytic degradation efficiency of non-steroidal anti-inflammatory drug (NSAIDs) using magnetically separable magnesium ferrite ($MgFe_2O_4$) nanoparticles. *Clean Technol. Environ. Policy* **2024**, 1–14. [CrossRef]
20. Hassadee, A.; Jutarosaga, T.; Onreabroy, W. Effect of zinc substitution on structural and magnetic properties of cobalt ferrite. *Procedia Eng.* **2012**, *32*, 597–602. [CrossRef]
21. Sajjia, M.; Oubaha, M.; Hasanuzzaman, M.; Olabi, A.G. Developments of cobalt ferrite nanoparticles prepared by the sol–gel process. *Ceram. Int.* **2014**, *40*, 1147–1154. [CrossRef]
22. Sajjia, M.; Oubaha, M.; Prescott, T.; Olabi, A.G. Development of cobalt ferrite powder preparation employing the sol–gel technique and its structural characterization. *J. Alloys Compd.* **2010**, *506*, 400–406. [CrossRef]
23. Jeevanantham, B.; Song, Y.; Choe, H.; Shobana, M.K. Structural and optical characteristics of cobalt ferrite nanoparticles. *Mater. Lett. X* **2021**, *12*, 100105. [CrossRef]
24. Banerjee, S.; John, V.T.; McPherson, G.L.; O'Connor, C.J.; Buisson, Y.S.L.; Akkarra, J.A.; Kaplan, D.L. Polymer microsphere and polymer-ferrite nanocomposite preparation by precipitation from water-in-oil microemulsions. *Coll. Polym. Sci.* **1997**, *275*, 930–937. [CrossRef]
25. Riaz, U.; Ashraf, S.M.; Raza, R.; Kohli, K.; Kashyap, J. Sonochemical Facile Synthesis of Self-Assembled Poly(o-phenylenediamine)/Cobalt Ferrite Nanohybrid with Enhanced Photocatalytic Activity. *Ind. Eng. Chem. Res.* **2016**, *55*, 6300–6309. [CrossRef]
26. Vinosha, P.A.; Das, J. Investigation on the role of pH for the structural, optical and magnetic properties of cobalt ferrite nanoparticles and its effect on the photo-fenton activity. *Mater. Today Proceed.* **2018**, *5*, 8662–8671. [CrossRef]
27. Le, T.-H.; Kim YYoon, H. Electrical and electrochemical properties of conducting polymers. *Polymers* **2017**, *9*, 150. [CrossRef] [PubMed]
28. Xiong, P.; Chen, Q.; He, M.; Sun, X.; Wang, X. Cobalt ferrite–polyaniline heteroarchitecture: A magnetically recyclable photocatalyst with highly enhanced performances. *J. Mater. Chem.* **2012**, *22*, 17485. [CrossRef]
29. Ghosh, S.; Mallik, A.K.; Basu, R.N. Enhanced photocatalytic activity and photoresponse of poly(3,4-ethylenedioxythiophene) nanofibers decorated with gold nanoparticles under visible light. *Sol. Energy* **2018**, *159*, 548–560. [CrossRef]
30. Ghosh, S.; Kouame, N.A.; Remita, S.; Ramos, L.; Goubard, F.; Aubert, P.-H.; Dazzi, A.; Deniset-Besseau, A.; Remita, H. Visible-light active conducting polymer nanostructures with superior photocatalytic activity. *Sci. Rep.* **2015**, *5*, 18002. [CrossRef]
31. Zhou, Q.; Shi, G. Conducting polymer-based catalysts. *J. Am. Chem. Soc.* **2016**, *138*, 2868–2876. [CrossRef] [PubMed]
32. Wang, D.; Zhang, J.; Luo, Q.; Li, X.; Duan, Y.; An, J. Characterization and photocatalytic activity of poly(3-hexylthiophene)-modified TiO2 for degradation of methyl orange under visible light. *J. Hazard. Mater.* **2009**, *169*, 546–550. [CrossRef] [PubMed]
33. Jana, B.; Bhattacharyya, S.; Patra, A. Conjugated polymer P3HT–Au hybrid nanostructures for enhancing photocatalytic activity. *Phys. Chem. Chem. Phys.* **2015**, *17*, 15392–15399. [CrossRef] [PubMed]
34. Leng, C.; Wei, J.; Liu, Z.; Xiong, R.; Pan, C.; Shi, J. Facile synthesis of PANI-modified $CoFe_2O_4$–TiO_2 hierarchical flower-like nanoarchitectures with high photocatalytic activity. *J. Nanopart. Res.* **2013**, *15*, 1643. [CrossRef]
35. Sadeghpour, F.; Nabiyouni, G.; Ghanbari, D. Simple synthesis of conductive poly aniline/cobalt ferrite magnetic nanocomposite: Its radio waves absorption and photo catalyst ability. *J. Clust. Sci.* **2022**, *33*, 1257–1266. [CrossRef]
36. Jung, H.-R.; Kim, K.N.; Lee, W.-J. Heterostructured $Co_{0.5}Mn_{0.5}Fe_2O_4$-polyaniline nanofibers: Highly efficient photocatalysis for photodegradation of methyl orange. *Korean J. Chem. Eng.* **2019**, *36*, 807–815. [CrossRef]